Robotica (2021), **39**, pp. 2268–2282
doi:10.1017/S026357472100031X

CAMBRIDGE UNIVERSITY PRESS

RESEARCH ARTICLE

Multi-objective optimal design of a novel 6-DOF spray-painting robot

Jun Wu[1,2*], Xiaojian Wang[1,2], Binbin Zhang[1,2] and Tian Huang[3,4]

[1]State Key Laboratory of Tribology and Institute of Manufacturing Engineering, Department of Mechanical Engineering, Tsinghua University, Beijing 100084, China, [2]Beijing Key Lab of Precision/Ultra-Precision Manufacturing Equipment and Control, Beijing 100084, China, [3]Key Laboratory of Mechanism Theory and Equipment Design of Ministry of Education, Tianjin University, Tianjin 300354, China and [4]School of Engineering, University of Warwick, Coventry CV4 7AL, UK
*Corresponding author. Email: jhwu@mail.tsinghua.edu.cn

Received: 4 September 2020; **Revised:** 6 March 2021; **Accepted:** 7 March 2021; **First published online:** 19 April 2021

Keywords: Hybrid robot, Performance evaluation, Compactness, Motion/force transmissibility, Energy consumption, Multi-objective optimization

Abstract

This paper deals with the multi-objective optimal design of a novel 6-degree of freedom (DOF) hybrid spray-painting robot. Its kinematic model is obtained by dividing it into serial and parallel parts. The dynamic equation is formulated by virtual work principle. A performance index for evaluating the compactness of robot is presented. Taking compactness, motion/force transmissibility, and energy consumption as performance indices, the optimal geometric parameters of the robot are selected in the Pareto-optimal set by constructing a comprehensive performance index. This paper is very useful for the development of the spray-painting robot.

1. Introduction

Automobile body painting is one of the four major processes in automobile manufacturing, which has an important effect on the quality of automobiles. Because of the advantages of high precision, high flexibility, and high quality, spray-painting robots have gradually replaced traditional spraying tools and attract more and more attention from industrial and academic fields. Most of the spray-painting robots are serial robots with big workspace. Compared with the serial robot, the parallel robot has high rigidity and strong carrying capacity. [1, 2, 3, 4] Moreover, the motors of the parallel robot are usually installed on the base, which reduces the inertia of the mobile body. However, parallel robots have small workspace. [5, 6, 7, 8] Taking the advantages of both serial and parallel robots into account, the hybrid robot is a better choice for spraying application.

Optimal design is an important step to improve robot performance. Since practical engineering applications often put forward multiple performance requirements for the robot, multi-objective optimization has been extensively studied. The classical multi-objective optimization method is to convert the multi-objective problem into a single-objective problem. [9, 10] A simple strategy to convert the multi-objective problem into a single-objective problem is to take the weighted sum of multiple objective functions as a single-objective function. However, it is usually difficult to establish an effective comprehensive objective function because different objective functions have different dimension and magnitude. In addition, users cannot know how optimal the result is because the relationship between design parameters and performance indices is unknown. [11] Multi-objective optimization based on Pareto-optimal solution is to improve a certain performance without reducing other performances, which can take various optimization objectives into account. [12, 13] From the Pareto-optimal set, we can know

about the relationships between different performance indices and how optimal the result is. Ridha Kelaiaia et al. [14] used Pareto-optimal principle to select the design parameters of the 2-degree of freedom (DOF) PAR2 parallel robot and successfully balanced the contradiction between the workspace and the kinematic performance. However, since Pareto-optimal set includes a series of solutions that cannot be considered better than the others according to Pareto-optimal principle, the selection of the final solution depends on the subjective experience of designers.

In this paper, a novel 6-DOF spray-painting robot with hybrid mechanism for automobile spraying is proposed, and its multiple-objective optimal design is investigated. Taking the robot compactness, motion/force transmissibility, and energy consumption into account, the optimum design based on Pareto-optimal solution is studied. The optimal geometric parameters of the spray-painting robot are determined by the NSGA-II algorithm based on Pareto-optimal solution.

The rest of this paper is organized as follows: Section 2 formulates the kinematic and dynamic model of the hybrid robot. In Section 3, the motion/force transmissibility and good transmission workspace (GTW) of the robot are analyzed and the performance indices for evaluating the compactness, transmission performance, and energy consumption are given in Section 4. Section 5 investigates the multi-objective optimization based on Pareto-optimal solution. Conclusions are presented in Section 6.

2. Kinematic and dynamic analysis

2.1. Structure description

Considering the advantages and disadvantages of parallel robots and serial robots, the hybrid robot that combines the advantages of the serial robot and the parallel robot is one of the ideal configurations for the spray-painting robot. Thus, a novel 6-DOF hybrid spray-painting robot is proposed for automobile spraying, which consists of a 3-DOF serial rotating base and a 3-DOF planar parallel mechanism. As shown in Fig. 1, the 3-DOF serial rotating base consists of frame, the lower base, the waist base, and the upper base which are sequentially connected by three revolute joints (J, K, and L). The planar parallel mechanism that is serially installed on the rotating base is composed of a 5R mechanism and a 2-parallelogram mechanism. The motor is fixed on the base and the mobile inertia is reduced.

Link AB and link ED are driven by servo motors to change the position of the spray gun CP through the 5R mechanism, and link AF is driven by a servo motor to determine the pose of the spray gun CP through the 2-parallelogram mechanism. The axes of the revolute joints ($A \sim I$) in planar parallel mechanism are parallel to each other. To describe the components of the robot, body fixed coordinate systems $\{1\} \sim \{12\}$ with reference to the rules of Denavit-Hartenberg (D-H) method as shown in Fig. 1(b) are established. The reference coordinate system $\{0\}$ is established at point K with Y_0 axis being vertical, Z_0 axis coincident with the axis of the rotatory joint attached to the frame, and X_0 axis satisfying the right-hand rule. The rotation matrix of coordinate system $\{i\}$ relative to the reference coordinate system $\{0\}$ is denoted by ${}^0_iR$.

2.2. Inverse kinematics of the planar parallel mechanism

As shown in Fig. 1(b), the planar parallel mechanism is in the O_3-X_3Z_3 plane. In Fig. 1(b), β_1, β_2, and γ are, respectively, the angles of link AB, link ED, and link AF relative to the X_3 axis. φ_1 and φ_2 are angles of links BC and DC relative to the links AB and ED, respectively. The angle between links BC and DC is φ_3 which is positive when BC is above DC. η_1 and η_2 are the angles in the 2-parallelogram mechanism. ε and δ are the structural parameters of the links. r_1, r_2, r_3, and r_4 are the length of links AB, ED, BC, and DC. r_5 is half of the length of AE. r_0 is the length of the spray gun CP.

Let $({}^3x_P, {}^3z_P)$ be coordinates of point P and η be the angle between CP and X_3 axis, driving angle γ and coordinates of point C can be expressed as

https://doi.org/10.1017/S026357472100031X Published online by Cambridge University Press

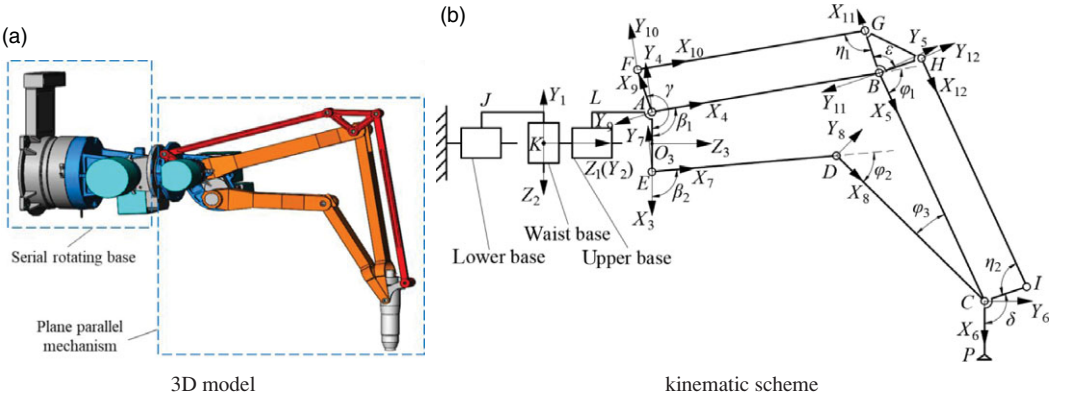

Figure 1. *The 6-DOF hybrid spray-painting robot.*

$$\gamma = \eta + \varepsilon + \delta \tag{1}$$

$$\left[{}^3x_C \;\; {}^3z_C \right] = \left[{}^3x_P - r_0 \cos\eta \quad {}^3z_P - r_0 \sin\eta \right] \tag{2}$$

The closed-loop constraint equation involved with the 5R mechanism in the planar parallel mechanism can be expressed as

$$\overline{OC} = \overline{OA} + \overline{AB} + \overline{BC} \tag{3}$$

$$\overline{OC} = \overline{OE} + \overline{ED} + \overline{DC} \tag{4}$$

Eqs. (3) and (4) can be written in component form as

$$\left[{}^3x_C \;\; {}^3z_C \right] = \left[-r_5 + r_1 \cos\beta_1 + r_3 \cos(\beta_1 + \varphi_1) \quad r_1 \sin\beta_1 + r_3 \sin(\beta_1 + \varphi_1) \right] \tag{5}$$

$$\left[{}^3x_C \;\; {}^3z_C \right] = \left[r_5 + r_2 \cos\beta_2 + r_4 \cos(\beta_2 + \varphi_2) \quad r_2 \sin\beta_2 + r_4 \sin(\beta_2 + \varphi_2) \right] \tag{6}$$

Based on Eqs. (5) and (6), the following equation can be obtained as

$$({}^3x_C - r_1 \cos\beta_1 + r_5)^2 + ({}^3z_C - r_1 \sin\beta_1)^2 = r_3^2 \tag{7}$$

$$({}^3x_C - r_2 \cos\beta_2 - r_5)^2 + ({}^3z_C - r_2 \sin\beta_2)^2 = r_4^2 \tag{8}$$

Based on Eqs. (7) and (8), the driving angles β_1 and β_2 can be obtained as

$$\beta_i = 2 \arctan\left(\frac{-b_i + \sigma_i \sqrt{b_i^2 - 4a_i c_i}}{2a_i} \right), \quad i = 1, 2 \tag{9}$$

where

$$\sigma_i = 1 \;\; or \; -1, a_1 = ({}^3x_C + r_5)^2 + {}^3z_C^2 + r_1^2 - r_3^2 + 2r_1({}^3x_C + r_5),$$

$$b_1 = -4{}^3z_C r_1, c_1 = ({}^3x_C + r_5)^2 + {}^3z_C^2 + r_1^2 - r_3^2 - 2r_1({}^3x_C + r_5),$$

$$a_2 = ({}^3x_C - r_5)^2 + {}^3z_C^2 + r_2^2 - r_4^2 + 2r_2({}^3x_C - r_5), b_2 = -4{}^3z_C r_2,$$

$$c_2 = ({}^3x_C - r_5)^2 + {}^3z_C^2 + r_2^2 - r_4^2 - 2r_2({}^3x_C - r_5)$$

From Eq. (9), it can be seen that there are four solutions for the inverse kinematics of the 5R mechanism. The four solutions correspond to four work modes, as shown in Fig. 2. The 5R mechanism in the spray-painting robot studied in this paper works in the "+ +" mode.

https://doi.org/10.1017/S026357472100031X Published online by Cambridge University Press

Table I. *D-H parameters of the equivalent serial robot.*

Parameter	a_{i-1}	α_{i-1}	d_i	θ_i
1	0	0	0	θ_1
2	90°	0	0	θ_2
3	−90°	0	d_3	θ_3
4	90°	a_4	0	θ_4
5	0	a_5	0	θ_5
6	0	a_6	0	θ_6

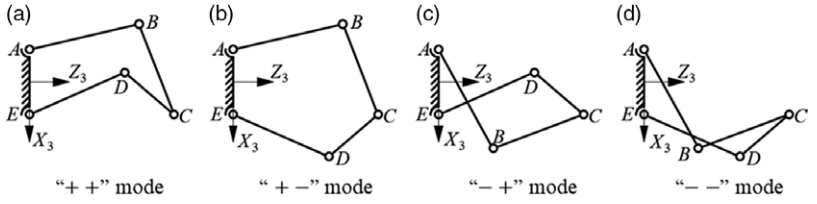

Figure 2. *The four inverse kinematic modes.*

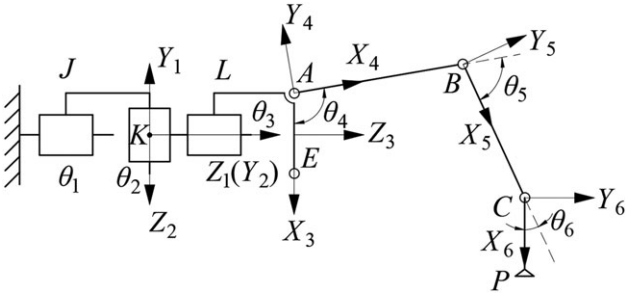

Figure 3. *Kinematic schematic diagram of equivalent serial robot.*

Then, φ_1, φ_2, and φ_3 can be obtained by Eqs. (5) and (6) as

$$\varphi_1 = \text{atan2}({}^3z_C - r_1 \sin\beta_1, {}^3x_C + r_5 - r_1\cos\beta_1) - \beta_1 \tag{10}$$

$$\varphi_2 = \text{atan2}({}^3z_C - r_2 \sin\beta_2, {}^3x_C - r_5 - r_2\cos\beta_2) - \beta_2 \tag{11}$$

$$\varphi_3 = \beta_2 + \varphi_2 - \beta_1 - \varphi_1 \tag{12}$$

2.3. Inverse kinematics of the hybrid robot

The hybrid robot is composed of a 3-DOF planar parallel mechanism and a 3-DOF serial mechanism. When the kinematics of the hybrid robot is studied, the parallel part can be regarded as a 3-DOF serial mechanism, and the kinematic model of the 6-DOF equivalent serial robot can be formulated using the D-H method. Body fixed coordinate systems {1}∼{6} as shown in Fig. 3 are established.

The D-H parameters describing the pose relationship between adjacent body fixed coordinate systems are listed in Table I, where $d_3 = 420$ mm, $a_4 = -r_5$, $a_5 = r_1$, and $a_6 = r_3$. $\theta_1 \sim \theta_6$ are the joint rotation angles of equivalent serial robots.

The homogeneous transformation matrices between adjacent body fixed coordinate systems are denoted by ${}^0_1T \sim {}^5_6T$, then the matrix of position and posture for the spray gun can be expressed as

https://doi.org/10.1017/S026357472100031X Published online by Cambridge University Press

$$ {}^{0}_{6}T = {}^{0}_{1}T\,{}^{1}_{2}T\,{}^{2}_{3}T\,{}^{3}_{4}T\,{}^{4}_{5}T\,{}^{5}_{6}T \tag{13} $$

When the inverse kinematics of the spray-painting robot is derived, the position of the spray gun and the axis direction of the spray gun are known, but the specific position of the spray gun around its axis is unknown. Thus, only 5-DOF of the spray gun can be determined and the robot has a redundant drive shaft. In order to simplify the analysis, it is assumed that the revolute joint connecting the frame and the lower base is the redundant drive shaft, which is not moved when the spray gun is in regular motion. Then the matrix of position and posture for the spray gun can be rewritten as

$$ {}^{0}_{6}T = {}^{1}_{6}T = {}^{1}_{2}T\,{}^{2}_{3}T\,{}^{3}_{4}T\,{}^{4}_{5}T\,{}^{5}_{6}T \tag{14} $$

Let $[\,n_x\ n_y\ n_z\,]^T$ be the axis direction of the spray gun in $\{0\}$, and $p_P = [\,p_x\ p_y\ p_z\,]^T$ be the position of the end of the spray gun in $\{0\}$. The position of point C in $\{0\}$ can be expressed as

$$ p_C = [\,x\ y\ z\,]^T = [\,p_x - r_0 n_x \quad p_y - r_0 n_y \quad p_z - r_0 n_z\,]^T \tag{15} $$

According to the physical meaning of ${}^{1}_{6}T$, it can be expressed as

$$ {}^{1}_{6}T = \begin{bmatrix} n_x & o_x & a_x & x \\ n_y & o_y & a_y & y \\ n_z & o_z & a_z & z \\ 0 & 0 & 0 & 1 \end{bmatrix} \tag{16} $$

where o_x, o_y, o_z, a_x, a_y, and a_z are unknown.

By multiplying the inverse matrix of ${}^{1}_{2}T \sim {}^{5}_{6}T$ on both sides of Eq. (14) in sequence and observing the characteristics of the corresponding elements on both sides, the joint rotation angles of equivalent serial robots can be obtained in sequence as

$$ \begin{aligned} &\theta_2 = \operatorname{atan2}(n_y x - n_x y, n_z y - n_y z), \quad \theta_3 = \operatorname{atan2}(y, xc\theta_2 + zs\theta_2) \\ &\theta_5 = -\arccos\left(\frac{(zc\theta_2 - d_3 - xs\theta_2)^2 + (ys\theta_3 - a_4 + xc\theta_2 c\theta_3 + zs\theta_2 c\theta_3)^2 - a_5^2 - a_6^2}{2a_5 a_6}\right) \\ &\theta_4 = \arccos\left(\frac{k_{11} a_6 s\theta_5 + k_{12}(a_5 + a_6 c\theta_5)}{k_{11}^2 + k_{12}^2}\right), \quad \theta_6 = atan2(k_{22}, k_{21}) \end{aligned} \tag{17} $$

where $k_{11} = zc\theta_2 - d_3 - xs\theta_2$, $k_{12} = ys\theta_3 - a_4 + xc\theta_2 c\theta_3 + zs\theta_2 c\theta_3$,

$$ \begin{aligned} k_{21} = {} & nc\theta_2 c\theta_4 s\theta_5 + nc\theta_2 s\theta_4 c\theta_5 + ms\theta_3 c\theta_4 c\theta_5 - ms\theta_3 s\theta_4 s\theta_5 - ls\theta_2 c\theta_4 s\theta_5 - ls\theta_2 s\theta_4 c\theta_5 \\ & + ns\theta_2 c\theta_3 c\theta_4 c\theta_5 - ns\theta_2 c\theta_3 s\theta_4 s\theta_5 + lc\theta_2 c\theta_3 c\theta_4 c\theta_5 - lc\theta_2 c\theta_3 s\theta_4 s\theta_5, \\ k_{22} = {} & nc\theta_2 c\theta_4 c\theta_5 - nc\theta_2 s\theta_4 s\theta_5 - ms\theta_3 c\theta_4 s\theta_5 - ms\theta_3 s\theta_4 c\theta_5 - ls\theta_2 c\theta_4 c\theta_5 + ls\theta_2 s\theta_4 s\theta_5 \\ & - ns\theta_2 c\theta_3 c\theta_4 s\theta_5 - ns\theta_2 c\theta_3 s\theta_4 c\theta_5 - lc\theta_2 c\theta_3 c\theta_4 s\theta_5 - lc\theta_2 c\theta_3 s\theta_4 c\theta_5. \end{aligned} $$

Then as shown in Fig. 1(b), β_1, γ, and φ_1 can be expressed as

$$ \begin{cases} \beta_1 = \theta_4 \\ \varphi_1 = \theta_5 \\ \gamma = \theta_4 + \theta_5 + \theta_6 + \varepsilon + \delta \end{cases} \tag{18} $$

The coordinates of point C in coordinate system O_3-X_3Z_3, which is represented by $({}^3x_C, {}^3z_C)$, can be obtained by Eq. (5). Then β_2 can be obtained by Eq. (8) as

$$ \beta_2 = \pi - \arcsin\left(\frac{h_3}{\sqrt{h_1^2 + h_2^2}}\right) - \arctan\frac{h_2}{h_1} \tag{19} $$

https://doi.org/10.1017/S026357472100031X Published online by Cambridge University Press

where $h_1 = 2^3z_C r_2$, $h_2 = 2r_2({}^3x_C - r_5)$ and $h_3 = {}^3x_C^2 + {}^3z_C^2 + r_2^2 - r_4^2 + r_5^2 - 2^3x_C r_5$. And φ_2 can be expressed by Eq. (6) as

$$\varphi_2 = \text{atan2}({}^3z_C - r_2 \sin\beta_2, {}^3x_C - r_5 - r_2\cos\beta_2) - \beta_2 \tag{20}$$

2.4. *Inverse dynamics of the hybrid robot*

The joint velocity and acceleration of the equivalent robot shown in Fig. 3 can be obtained by taking the time derivative of the corresponding joint position. The angular velocity and origin velocity of coordinate system {1} can be expressed as

$$\boldsymbol{\omega}_1 = \begin{bmatrix} 0 \\ 0 \\ \dot{\theta}_1 \end{bmatrix} = \boldsymbol{J}_{\omega 1}\dot{\boldsymbol{\Theta}}, \boldsymbol{v}_1 = \begin{bmatrix} 0 \\ 0 \\ 0 \end{bmatrix} = \boldsymbol{J}_{v1}\dot{\boldsymbol{\Theta}} \tag{21}$$

where $\boldsymbol{J}_{\omega 1} = \begin{bmatrix} 0\,0\,0\,0\,0\,0 \\ 0\,0\,0\,0\,0\,0 \\ 1\,0\,0\,0\,0\,0 \end{bmatrix}$, $\dot{\boldsymbol{\Theta}} = [\dot{\theta}_1\ \ \dot{\theta}_2\ \ \dot{\theta}_3\ \ \dot{\theta}_4\ \ \dot{\theta}_5\ \ \dot{\theta}_6]^T$ and $\boldsymbol{J}_{v1}$ is a 3×6 null matrix. The angular velocity and origin velocity of the remaining body fixed coordinate systems can be obtained using the speed superposition principle. For instance, the angular velocity and origin velocity of coordinate system {2} can be obtained as

$$\boldsymbol{\omega}_2 = \boldsymbol{\omega}_1 + {}^0_2\boldsymbol{R}\begin{bmatrix} 0 \\ 0 \\ \dot{\theta}_2 \end{bmatrix} = \boldsymbol{J}_{\omega 2}\dot{\boldsymbol{\Theta}}, \boldsymbol{v}_2 = \boldsymbol{v}_1 + \boldsymbol{\omega}_1 \times {}^0_1\boldsymbol{R}^1\boldsymbol{P}_2 = \boldsymbol{J}_{v2}\dot{\boldsymbol{\Theta}} \tag{22}$$

where $\boldsymbol{J}_{\omega 2} = \boldsymbol{J}_{\omega 1} + {}^0_2\boldsymbol{R}\boldsymbol{J}_{m2}, \boldsymbol{J}_{m2} = \begin{bmatrix} 0\,0\,0\,0\,0\,0 \\ 0\,0\,0\,0\,0\,0 \\ 0\,1\,0\,0\,0\,0 \end{bmatrix}, \boldsymbol{J}_{v2} = \boldsymbol{J}_{v1} - \left[\left({}^0_1\boldsymbol{R}^1\boldsymbol{P}_2\right)\times\right]\boldsymbol{J}_{\omega 1}$ and ${}^1\boldsymbol{P}_2$ represents the position vector from the origin of coordinate system {1} to the origin of coordinate system {2} in coordinate system {1}. $[\boldsymbol{w}\times] = \begin{bmatrix} 0 & -w_{3z} & w_{3y} \\ w_{3z} & 0 & -w_{3x} \\ -w_{3y} & w_{3x} & 0 \end{bmatrix}$ denotes the skew-symmetric matrix of $\boldsymbol{w}$. Similarly, the angular velocity and origin velocity of the other body fixed coordinate systems can be obtained as

$$\boldsymbol{\omega}_{\text{i}} = \boldsymbol{J}_{\omega \text{i}}\dot{\boldsymbol{\Theta}}, \boldsymbol{v}_{\text{i}} = \boldsymbol{J}_{\text{vi}}\dot{\boldsymbol{\Theta}}, i = 3 \sim 12 \tag{23}$$

Given the angular velocity and origin velocity of the body fixed coordinate system, the velocity of the mass center of the component can be expressed as

$$\boldsymbol{v}_{Ci} = \boldsymbol{v}_i + \boldsymbol{\omega}_i \times {}^0_i\boldsymbol{R}^i\boldsymbol{P}_{Ci} = \boldsymbol{J}_{\text{vci}}\dot{\boldsymbol{\Theta}}, i = 1 \sim 12 \tag{24}$$

where $\boldsymbol{J}_{vci} = \boldsymbol{J}_{vi} - [({}^0_i\boldsymbol{R}^i\boldsymbol{P}_{Ci}) \times]\boldsymbol{J}_{\omega i}$ and ${}^i\boldsymbol{P}_{Ci}$ is the position vector of the mass center C_i of component i in body fixed coordinate system $\{i\}$. By taking the time derivative of Eqs. (21)∼(24), the angular acceleration which is denoted by $\dot{\boldsymbol{\omega}}_{\text{i}}$, the origin acceleration which is denoted by $\dot{\boldsymbol{v}}_{\text{i}}$, and the acceleration of mass center which is denoted by $\dot{\boldsymbol{v}}_{\text{Ci}}$ can be obtained.

The gravity and inertial force acting on the mass center of the component i can be expressed as

$$\boldsymbol{F}_{\text{i}} = \text{m}_{\text{i}}\boldsymbol{g} - \text{m}_{\text{i}}\dot{\boldsymbol{v}}_{\text{Ci}} \tag{25}$$

The inertial torque about mass center acting on the component i can be expressed as

$$\boldsymbol{T}_{\text{i}} = -\boldsymbol{I}_{\text{Ci}}\dot{\boldsymbol{\omega}}_{\text{i}} - \boldsymbol{\omega}_{\text{i}} \times (\boldsymbol{I}_{\text{Ci}}\boldsymbol{\omega}_{\text{i}}) \tag{26}$$

where $\boldsymbol{I}_{Ci} = {}^0_i\boldsymbol{R}\boldsymbol{I}'_{Cii}{}^0\boldsymbol{R}^T$ and $\boldsymbol{I}'_{Ci}$ is the inertia matrix of component i referred by mass center in mass center coordinate.

https://doi.org/10.1017/S026357472100031X Published online by Cambridge University Press

Taking the time derivative of Eqs. (18) and (19), the mapping between the actual driving angle rate and the joint angle rate of equivalent serial robot can be expressed as

$$\dot{\boldsymbol{q}} = \boldsymbol{J}_{\mathrm{q}}\dot{\boldsymbol{\Theta}} \tag{27}$$

where $\dot{\boldsymbol{q}} = [\dot{\theta}_1 \ \ \dot{\theta}_2 \ \ \dot{\theta}_3 \ \ \dot{\beta}_1 \ \ \dot{\beta}_2 \ \ \dot{\gamma}]^T$ and $\boldsymbol{J}_q$ is the Jacobi matrix.

Let $\boldsymbol{\tau} = [\,\tau_1 \ \tau_2 \ \tau_3 \ \tau_4 \ \tau_5 \ \tau_6\,]^T$ be the driving torque vector, the virtual work principle yields

$$\sum_{i=1}^{12} \left(\delta \boldsymbol{v}_{Ci}^T \boldsymbol{F}_i + \delta \boldsymbol{\omega}_i^T \boldsymbol{T}_i\right) + \delta \dot{\boldsymbol{q}}^{\mathrm{T}} \boldsymbol{\tau} = 0 \tag{28}$$

Substituting $\delta \boldsymbol{v}_{\mathrm{Ci}} = \boldsymbol{J}_{\mathrm{vci}} \delta \dot{\boldsymbol{\Theta}}$, $\delta \boldsymbol{\omega}_{\mathrm{i}} = \boldsymbol{J}_{\omega \mathrm{i}} \delta \dot{\boldsymbol{\Theta}}$, and $\delta \dot{\boldsymbol{q}} = \boldsymbol{J}_{\mathrm{q}} \delta \dot{\boldsymbol{\Theta}}$ into Eq. (28) leads to

$$\boldsymbol{\tau} = -\boldsymbol{J}_q^{-T} \sum_{i=1}^{12} \left(\boldsymbol{J}_{vci}^T \boldsymbol{F}_i + \boldsymbol{J}_{\omega i}^T \boldsymbol{T}_i\right) \tag{29}$$

3. Workspace analysis

In this section, the GTW of the planar parallel mechanism is investigated and then the whole workspace of the hybrid robot is determined.

3.1. GTW of planar parallel mechanism

It can be seen from Eq. (7) that if β_1 is specified, the workspace of the first limb is a circle. If β_1 ranges from 0 to 2π, the workspace of the limb is an annulus constrained by two circles $C_{1\mathrm{i}}$ with the radius of $(r_1 - r_3)$ and $C_{1\mathrm{o}}$ with the radius of $(r_1 + r_3)$. The workspace of the second limb is also an annulus, and the theoretical workspace of the 5R mechanism is the overlapping part of these two annuluses. In order to ensure that there is an overlap between the two annuluses, the structural parameters of the 5R mechanism need to meet the following conditions:

$$\begin{cases} r_1 + r_3 + r_2 + r_4 > 2r_5 \\ r_2 - r_4 < 2r_5 + r_1 + r_3 \\ r_1 - r_3 < 2r_5 + r_2 + r_4 \end{cases} \tag{30}$$

Considering the joint limitation and mechanism interference, the range of β_1 and β_2 should be [30°,150°] and [0°,180°], respectively. Usually, the largest continuous workspace is used as the usable workspace. Although there is not singular configuration in the usable workspace, the motion/force transmissibility of the mechanism will deteriorate when the mechanism is close to the singular configuration. To avoid poor motion/force transmissibility, the GTW is defined. The transmission angle is widely used to measure the motion/force transmissibility. When transmission angle is close to 90°, the mechanism is far away from the singular configuration, and the mechanism has good transmissibility. On the contrary, when the transmission angle is close to 0° or 180°, the mechanism is close to the singular configuration, and the mechanism has poor transmissibility. For high-speed motion, the most widely accepted range of transmission angle is [45°, 135°].[15] For the 5R mechanism in the spray-painting robot, since the end-effector is a light spray gun with slow velocity, the range [45°, 135°] is too conservative. Therefore, we can reasonably expand the acceptable transmission angle range. However, there is not a uniform standard for the transmission angle of spray-painting robots currently. As far as we know, the range [20°, 160°] is widely used by engineers in the spraying industry.[16] Therefore, GTW is defined as the workspace where all transmission angles related belong to [20°, 160°]. According to the definition of angle in Fig. 1(b), $-\varphi_1$, $-\varphi_2$, and φ_3 are the transmission angles of 5R mechanism. In the GTW, $-\varphi_1$, $-\varphi_2$, and φ_3 should belong to [20°,160°], that is, $-160° \le \varphi_1 \le -20°$, $-160° \le \varphi_2 \le -20°$, $20° \le \varphi_3 \le 160°$.

https://doi.org/10.1017/S026357472100031X Published online by Cambridge University Press

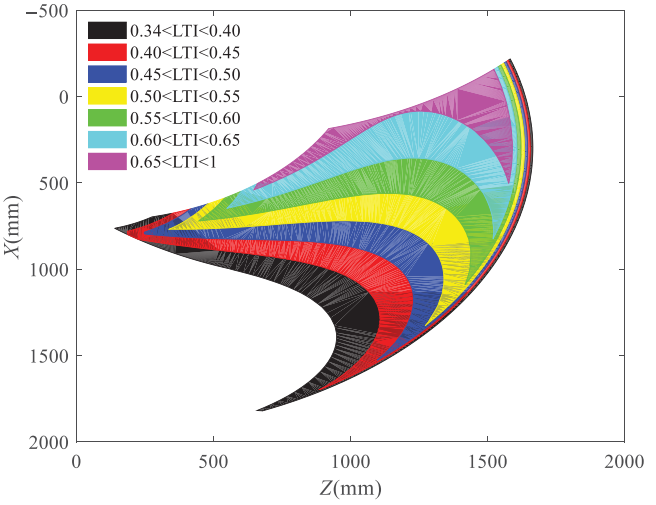

Figure 4. *GTW and transmissibility distribution.*

The range of φ_1 can ensure that links AB and BC will not interfere, the range of φ_2 can ensure that links ED and DC will not interfere, and the range of φ_3 can ensure that links BC and CD will not interfere. In addition, it should be ensured that links AB and ED will not interfere. If β_1 is specified, links AB and ED just interfere when B is on link ED, or D is on link AB. The abovementioned angle limitation of φ_3 can prevent the occurrence of the situation in which B is on link ED. When D is on link AB, links AB and ED just interfere, and β_2 can be expressed as

$$\beta_{2\,\max} = \operatorname{atan2}\left(\left(\frac{-b_3+\sqrt{b_3^2-4c_3}}{2}\right)\sin\beta_1, -2r_5+\left(\frac{-b_3+\sqrt{b_3^2-4c_3}}{2}\right)\cos\beta_1\right) \tag{31}$$

where $b_3 = -4r_5\cos\beta_1$ and $c_3 = 4r_5^2 - r_2^2$. If $b_3^2 - 4c_3 < 0$, it means that the configuration will not occur, then let $\beta_{2\,\max} = 180°$. If β_1 is specified, β_2 ranges from 0° to $\beta_{2\max}$. For example, if $r_1 = 1050$ mm, $r_2 = 650$ mm, $r_3 = 1450$ mm, $r_4 = 1040$ mm, and $r_5 = 300$ mm, the GTW of planar parallel mechanism can be figured out, as shown in Fig. 4.

3.2. GTW of hybrid robot

In the hybrid robot, the revolute joint corresponding to γ is mainly used to adjust the posture of the spray gun, so it is not considered to find the workspace. To simplify the analysis, we only consider the workspace associated with joint angles θ_2, θ_3, β_1, and β_2. The overall workspace can be obtained by rotating the workspace associated with the four joint angles about the axis of the revolute joint corresponding to θ_1. The GTW of hybrid robot can be obtained by using Monte Carlo method. Ten thousand points are randomly selected within the range of θ_2, θ_3, β_1, and β_2, where θ_2 belongs to $[-90°, 90°]$, θ_3 belongs to $[-180°, 180°]$, and the range of β_1 and β_2 is determined by the GTW of the planar parallel mechanism analyzed in Section 3.1. Then the position of point C can be calculated by the kinematic model of the hybrid robot to form the schematic diagram of the GTW of the hybrid robot.

4. Performance indices

4.1. Robot compactness

The workspace is usually the first performance to be concerned by designers. [17] Many researchers use the size of the workspace as an important index. [16, 18, 20] In addition, the volume of the space

https://doi.org/10.1017/S026357472100031X Published online by Cambridge University Press

occupied by the robot itself is also important for the spray-painting robot. The spraying workshop needs to reserve enough space for the movement of the robot body. Under the same conditions, the smaller the volume occupied by the robot body, the smaller the volume required for the spraying workshop. The reduction of the size of the spraying workshop can reduce the energy consumption of the spraying workshop for dust removal, temperature control, etc. Therefore, the space occupied by the robot itself should be as small as possible on the premise of ensuring that the size of the working space meets the requirements, which puts forward requirement on the compactness of robot. A performance index used to evaluate the compactness of the robot is defined as

$$\lambda = \frac{V_W}{V_O} \tag{32}$$

where V_W is the volume of the GTW and V_O is the volume of space that the robot needs to occupy during work. As shown in Fig. 1(b), one may see that points F, G, H, and I may be always located at the boundary of the space occupied by robot, so V_O can be described by the volume of the smallest convex polyhedron that can contain all possible positions of points F, G, H, and I.

4.2. Motion/Force transmissibility

In the serial part of the robot, since the revolute joints are directly driven by the motor, it can be considered that the transmission angle is always equal to 90°. In the parallel part of the robot, the definition of the GTW only deals with the transmission angles involved with the position of spray gun, but the transmission angles related to the posture of spray gun also affect the motion/force transmissibility. As shown in Fig. 1(b), the main transmission angles in the spray-painting robot are φ_1, φ_2, φ_3, η_1, and η_2. In order to quantitatively measure the motion/force transmissibility of the spray-painting robot at a certain position in GTW, the local transmission index is defined as

$$\mathrm{LTI} = \min\left\{\left|\sin\varphi_1\right|, \left|\sin\varphi_2\right|, \left|\sin\varphi_3\right|, \left|\sin\eta_1\right|, \left|\sin\eta_2\right|\right\} \tag{33}$$

To measure the average transmissibility in GTW, the global transmission index is defined as

$$\mathrm{GTI} = \frac{\int_{V_W} (\mathrm{LTI})\mathrm{d}V}{\int_{V_W} \mathrm{d}V} \tag{34}$$

For example, if $r_1 = 1050$mm, $r_2 = 650$mm, $r_3 = 1450$mm, $r_4 = 1040$mm, $r_5 = 300$mm, $\varepsilon = 90°$, and $\delta = 90°$, the distribution of transmissibility of the parallel mechanism is shown in Fig. 4. At the lower boundary of the workspace, the transmissibility of the mechanism is poor, which shows that the main reason for limiting the workspace in this area is that the mechanism is close to the singular configuration, while the transmissibility of the mechanism is still good at the upper boundary of the workspace, where the main reason for restricting the workspace of the mechanism is not the singular configuration, but the interference of the links.

4.3. Energy consumption

In the process of automobile production, the energy consumption of the spray workshop often accounts for a huge proportion of the energy consumption of the entire production line. Therefore, reducing the energy consumption in the spraying process can greatly reduce the energy consumption in the automobile production process and further achieve the purpose of reducing costs, energy saving, and environmental protection. This paper mainly focuses on the parameter optimization of the spray-painting robot, so the energy consumption in this paper mainly refers to the mechanical energy consumed by the

https://doi.org/10.1017/S026357472100031X Published online by Cambridge University Press

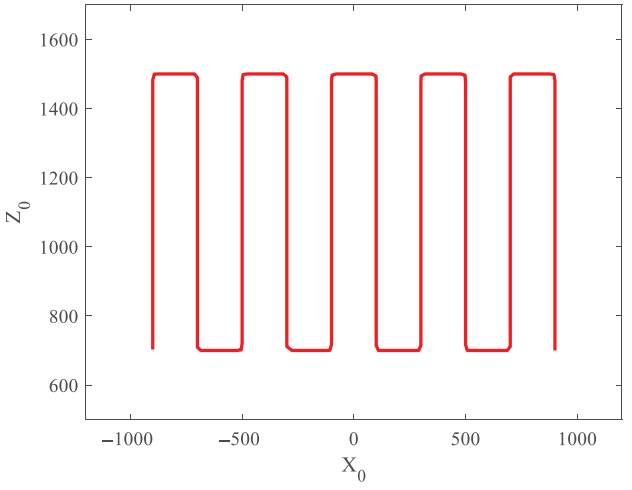

Figure 5. *Typical spraying trajectory.*

robot movement during the car spraying process. In the spraying production line, the spraying trajectories are often fixed, and the energy consumption for spraying can be reduced by optimizing the energy consumption for typical spraying trajectories.

The performance index for evaluating the energy consumption is defined as the energy consumed by the robot in a typical spray trajectory. During the spraying process, the power required by each motor can be expressed as [21, 22]

$$\mathrm{P_i} = \tau_\mathrm{i} \cdot \dot{\theta}_\mathrm{i} (i = 1 \sim 3), \mathrm{P}_4 = \tau_4 \cdot \dot{\beta}_1, \mathrm{P}_5 = \tau_5 \cdot \dot{\beta}_2, \mathrm{P}_6 = \tau_6 \cdot \dot{\gamma} \tag{35}$$

The work done by a single motor can be expressed as

$$E_i = \int_0^t |P_i| \, dt \tag{36}$$

The total energy consumed can be calculated by

$$E = \sum_{i=1}^{6} E_i \tag{37}$$

Taking the spraying process of the roof as an example, the straight trajectory is still the most typical and commonly used trajectory in practical production, so the typical electrostatic spraying trajectory of the roof used in the optimization is shown in Fig. 5. The adjacent straight segments are connected by a circular arc with radius of 10 mm. During the spraying process, the direction of the spray gun is always kept vertical, and the speed of the spray gun along the spray trajectory is always 400 mm/s.

5. Multi-objective optimization based on Pareto-optimal solution

5.1. Constraints for optimal design

In the painting production line, there are usually at least two robots installed on both sides of the vehicle. Therefore, each robot only needs to spray half of the vehicle. The largest spraying area is half of the roof area. This area can be regarded as a rectangle with a length of 2000 mm ($\overline{ST}$) and a width of 900 mm ($\overline{MQ}$). If the spray-painting robot can complete the painting of this area, it must be able to complete the painting of the vehicle.

Fig. 6 shows the installation parameters of the robot relative to the vehicle, where point K is the center of the arc SNT and is the intersection point of the serial joint axes of the hybrid spray-painting robot.

https://doi.org/10.1017/S026357472100031X Published online by Cambridge University Press

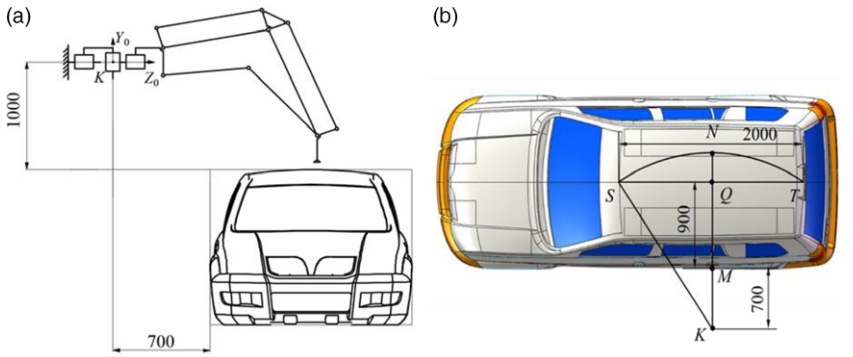

Figure 6. *Installation position of the robot and vehicle.*

The line segment $\overline{KM} = 700$ mm. Arc SNT is the smallest spraying arc that can cover the rectangular spraying area. Thus, the minimum spraying radius for the robot is $\overline{MN}$. The line segment $\overline{KS}$ in the triangle KSQ can be given as

$$\overline{KS} = \sqrt{\overline{KQ}^2 + \overline{SQ}^2} = \sqrt{(\overline{KM} + \overline{MQ})^2 + (\overline{ST}/2)^2} \tag{38}$$

According to Eq. (38), we can get $\overline{MN}$=1187mm. Therefore, in order to complete the spraying task, the radius of the spraying trace should not be less than 1187 mm. It means that the length of the workspace along the Z_3 axis at X_3=700 mm, which is denoted by $L_{X_3=700}$, should meet the condition $L_{X_3=700} \geq 1187$ mm.

5.2. Problem statement for multi-objective optimization

The multi-objective optimization of the robot is to determine the optimal dimensions which ensure the optimal performance as well as satisfy geometrical and technological constraints. The geometric parameters to be optimized include the angles ε, δ and the lengths of the five links in the 5R mechanism r_1, r_2, r_3, r_4, and r_5. The multi-objective optimization can be formulated as follows:

Find an optimal vector $X = [\, r_1 \; r_2 \; r_3 \; r_4 \; r_5 \; \varepsilon \; \delta \,]^T$ that

$$\min f(X) = \min[\, f_1 \; f_2 \; f_3 \,]^T = \min[\, -\mathrm{GTI} \; -\lambda \; E \,]^T \tag{39}$$

Subject to

$$\begin{cases} 200 \text{ mm} \leq r_1, r_2, r_3, r_4 \leq 2000 \text{ mm} \\ 100 \text{ mm} \leq r_5 \leq 500 \text{ mm} \\ 0^\circ \leq \varepsilon \leq 180^\circ \\ 0^\circ \leq \delta \leq 180^\circ \\ r_1 + r_3 + r_2 + r_4 > 2r_5 \\ r_2 - r_4 < 2r_5 + r_1 + r_3 \\ r_1 - r_3 < 2r_5 + r_2 + r_4 \\ L_{X_3=700} \geq 1187 \text{ mm} \end{cases}$$

https://doi.org/10.1017/S026357472100031X Published online by Cambridge University Press

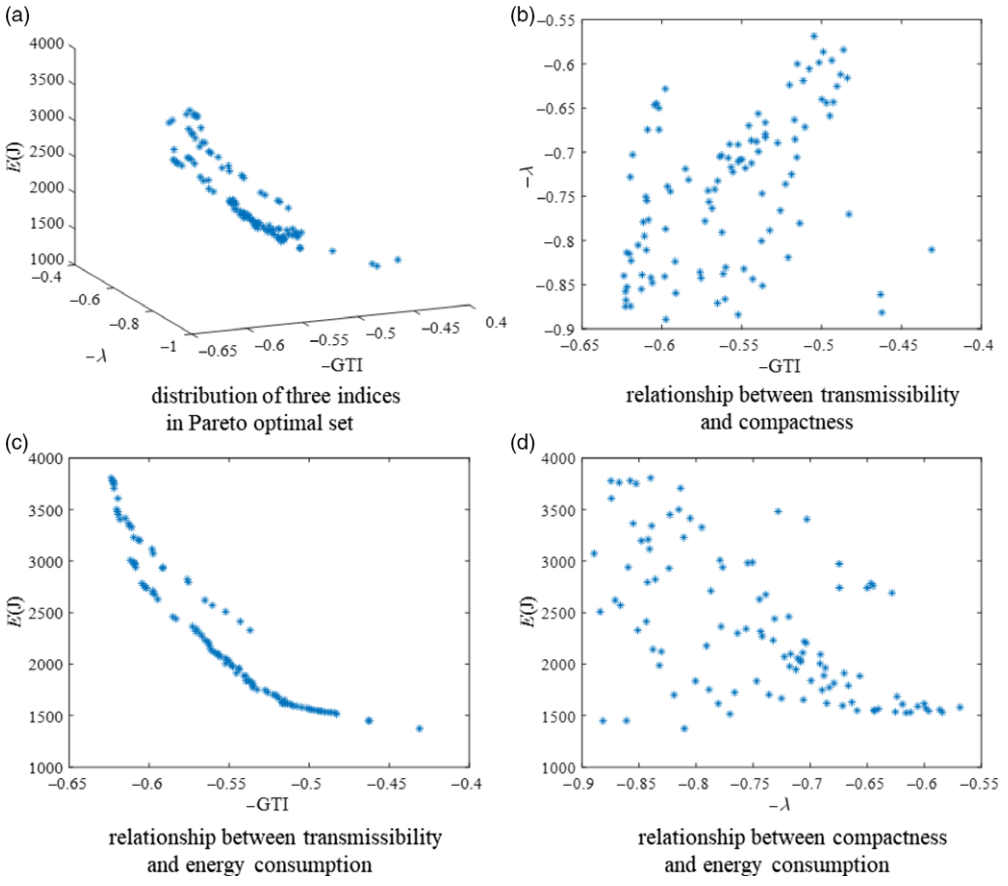

Figure 7. *Distribution of Pareto-optimal set.*

5.3. Final solution selection

Multi-objective optimization based on Pareto-optimal solution is to improve a certain performance without reducing other performance. The result is a series of solutions that cannot be considered better than the others according to Pareto-optimal principle. Non-dominated sorting genetic algorithm (NSGA) proposed in 1995 is an optimization algorithm used to obtain Pareto-optimal set. Later, the non-dominated sorting genetic algorithm with elite strategy (NSGA-II) is proposed, which is of better efficiency and simplicity compared with NSGA. [23]

MATLAB is used for implementation of the NSGA-II, with the following parameters: number of population = 200, number of generation = 200, crossing probability = 0.9, and probability of mutation = 0.1. Taking the compactness, transmissibility, and energy consumption into account, the optimum results are shown in Fig. 7. It can be seen from Fig. 7(b) that the relationship between the performance of transmissibility and compactness is complicated, not simple correlation. From Fig. 7(c), one may see that the improvement of the transmissibility often brings an increase in energy consumption, which shows the performance of transmissibility and energy consumption is conflicting. Fig. 7(d) shows that the relationship between the performance of compactness and energy consumption is complicated. In addition to analyzing the relationship between various performance indices, the results of the Pareto-optimal set can also help us avoid getting extreme result and know how optimal the result is.

In order to determine the final solution, the decision-maker needs to choose according to the focus of demand. In this paper, weights of different performance indices are assigned as shown in Table II. The

https://doi.org/10.1017/S026357472100031X Published online by Cambridge University Press

Table II. *Weights of different performance indices.*

Performance index	**GTI**	**λ**	***E***
Weight	0.3	0.3	0.4

Table III. *Parameters and performance indices of the final solution.*

r_1(mm)	r_2(mm)	r_3(mm)	r_4(mm)	r_5(mm)	ε(°)	δ(°)	GTI	λ	E(J)
1084.4	682.7	1369.4	1050.3	303.8	123.8	88.9	0.55	0.83	1985.8

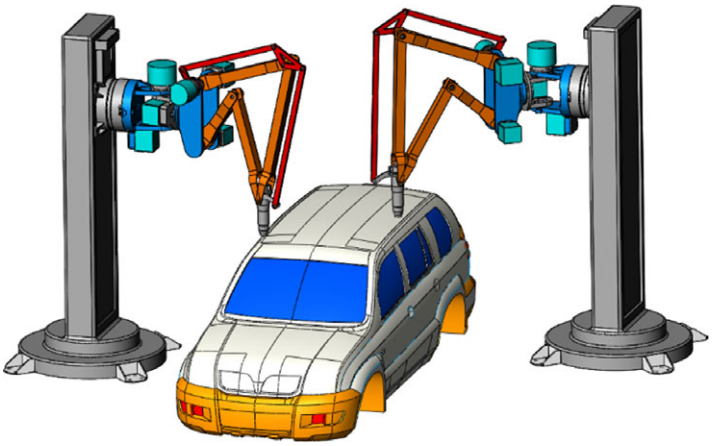

Figure 8. *Layout of the optimum spray-painting robot.*

weight of the performance index represents the importance of the performance index, and it is assigned based on the focus of practical needs and engineering experience of designers.

Although the solution in the Pareto-optimal set cannot be considered better than the other solutions in the set, the results of the Pareto-optimal set can be used to normalize the performance indices to solve the problem of non-uniformity of dimension and magnitude between different performance indices. Each performance index can be normalized as

$$\widetilde{f}_i = \frac{f_{i\max} - f_i}{f_{i\max} - f_{i\min}} \tag{40}$$

where $\widetilde{f}_i$ is the normalized performance index of f_i; $f_{i\max}$ and $f_{i\min}$ are the maximum and minimum values of the i-th performance index in the Pareto-optimal set, respectively. Next a comprehensive performance index through weighted calculation can be defined as

$$f = 0.3\widetilde{f}_1 + 0.3\widetilde{f}_2 + 0.4\widetilde{f}_3 \tag{41}$$

The larger the comprehensive performance index, the better the performance of the robot. Thus, the solution with the largest comprehensive performance index in the Pareto-optimal set is selected as the final solution, whose parameters and performance indices are shown in Table III.

Based on the optimized parameters, an optimum hybrid spray-painting robot is obtained, and the structural parameters not mentioned therein are determined according to the practical circumstance or the experience of the designer. In the production line, at least two robots are needed to paint the car, and the layout of the optimum hybrid spray-painting robot is shown in Fig. 8. The GTW and the distribution of transmissibility of the planar parallel mechanism of the spray-painting robot are shown in Fig. 9. Compared with the results shown in Fig. 4, one may see that the area where $0.65<\text{LTI}<1$ in workspace

https://doi.org/10.1017/S026357472100031X Published online by Cambridge University Press

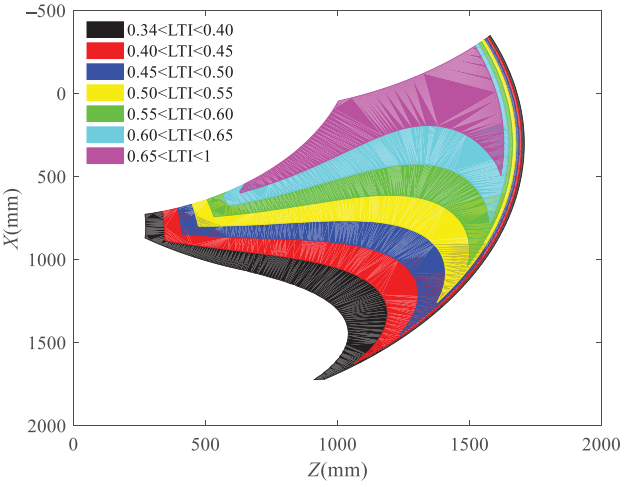

Figure 9. *Distribution of transmissibility of the optimum robot.*

shown in Fig. 9 is significantly increased, which indicates that the motion/force transmissibility of the optimum robot is significantly improved. Thus, the optimum design is effective.

6. Conclusion

A novel 6-DOF hybrid robot is proposed and the multi-objective optimal design of the robot is investigated by considering the compactness, motion/force transmissibility, and energy consumption. The kinematic model is obtained by dividing the robot into serial and parallel parts and the dynamic equation is formulated using virtual work principle. The GTW of the robot is analyzed considering the transmissibility and link interference. The Pareto-optimal set is calculated by NSGA-II algorithm. Based on the results of Pareto-optimal set, a comprehensive performance index is constructed and the optimum parameters are obtained as $r_1 = 1084.4$mm, $r_2 = 682.7$mm, $r_3 = 1369.4$mm, $r_4 = 1050.3$mm, $r_5 = 303.8$mm, $\varepsilon = 123.8°$, and $\delta = 88.9°$. The parameter optimization conducted in this paper improves the compactness and transmission performance of the robot, reduces the energy consumption in the typical trajectory, and makes the spray-painting robot have better comprehensive performance in actual application. This work is very useful for the development of the hybrid spray-painting robot.

Acknowledgments. This work is supported by the National Natural Science Foundation of China (Grant No. 51975321), EU H2020-MSCA-RISE-ECSASDPE (No. 734272) and Tianjin Key Laboratory of High Speed Cutting & Precision Machining.

Conflicts of Interest. The authors declare none.

References

[1] J. Wu, G. Yu, Y. Gao and L. P. Wang, "Mechatronics modeling and vibration analysis of a 2-DOF parallel manipulator in a 5-DOF hybrid machine tool," *Mech. Mach. Theory*. **121**, 430–445 (2018).

[2] D. S. Zhang, Y. D. Xu, J. T. Yao and Y. S. Zhao, "Analysis and optimization of a spatial parallel mechanism for a new 5-DOF hybrid serial-parallel manipulator," *Chin. J. Mech. Eng-En*. **31**(1), 54 (2018).

[3] J. Wu, J. S. Wang, L. P. Wang and T. M. Li, "Dynamics and control of a planar 3-DOF parallel manipulator with actuation redundancy," *Mech. Mach. Theory*. **44**(4), 835–849 (2009).

[4] Y. J. Zhao and F. Gao, "Dynamic performance comparison of the 8PSS redundant parallel manipulator and its non-redundant counterpart-the 6PSS parallel manipulator," *Mech. Mach. Theory*. **44**(5), 991–1008 (2009).

[5] M. K. Lee and K. W. Park, "Workspace and singularity analysis of a double parallel manipulator," *IEEE-ASME T. Mech.* **5**(4), 367–375 (2000).

[6] B. Zi, J. B, Cao, Z. C. Zhu and P. Mitrouchev, "Design, dynamics, and workspace of a hybrid-driven-based cable parallel manipulator," *Math. Probl. Eng*. **2013**, 914653 (2013).

https://doi.org/10.1017/S026357472100031X Published online by Cambridge University Press

[7] Y. D. Xu, J. T. Yao and Y. S. Zhao, "Inverse dynamics and internal forces of the redundantly actuated parallel manipulators," *Mech. Mach. Theory*. **51**, 172–184 (2012).
[8] D. S. Zhang, Y. D. Xu, J. T. Yao and Y. S. Zhao, "Design of a novel 5-DOF hybrid serial-parallel manipulator and theoretical analysis of its parallel part," *Robot. Cim-Int. Manuf.* **53**, 228–239 (2018).
[9] M. Stock and K. Miller, "Optimal kinematic design of spatial parallel manipulators: Application to linear delta robot," *J. Mech. Design.* **125**(2), 292–301 (2003).
[10] J. Ryu and J. Cha, "Volumetric error analysis and architecture optimization for accuracy of HexaSlide type parallel manipulators," *Mech. Mach. Theory*. **38**(3), 227–240 (2003).
[11] X. J. Liu and J. S. Wang, "A new methodology for optimal kinematic design of parallel mechanisms," *Mech. Mach. Theory*. **42**(9), 1210–1224 (2007).
[12] R. Kelaiaia, A. Zaatri and O. Company, "Multiobjective optimization of 6-dof UPS parallel manipulators," *Adv. Robotics* **26**(16), 1885–1913 (2012).
[13] R. Saravanan, S. Ramabalan and C. Balamurugan, "Evolutionary optimal trajectory planning for industrial robot with payload constraints," *Int. J. Adv. Manuf. Tech.* **38**(11–12), 1213–1226 (2008).
[14] R. Kelaiaia, A. Zaatri, O. Company and L. Chikh, "Some investigations into the optimal dimensional synthesis of parallel robots," *Int. J. Adv. Manuf. Tech*. **83**(9–12), 1525–1538 (2016).
[15] C. Wu, X. J. Liu, L. P. Wang and J. S. Wang, "Optimal design of spherical 5R parallel manipulators considering the motion/force transmissibility," *J. Mech. Design*. **132**(3), 031002 (2010).
[16] X. J. Liu, J. Li and Y. H. Zhou, "Kinematic optimal design of a 2-degree-of-freedom 3-parallelogram planar parallel manipulator," *Mech. Mach. Theory*. **87**, 1–17 (2015).
[17] J. Wu, Y. Gao, B. B. Zhang and L. P. Wang, "Workspace and dynamic performance evaluation of the parallel manipulators in a spray-painting equipment," *Robot. Cim-Int. Manuf.* **44**, 199–207 (2017).
[18] Y. Jin, Z. M. Bi, H. T. Liu, C. Higgins, M. Price, W. H. Chen and T. Huang, "Kinematic analysis and dimensional synthesis of Exechon parallel kinematic machine for large volume machining," *J. Mech. Robot*. **7**(4), 041004 (2015).
[19] E. Ottaviano and M. Ceccarelli, "Optimal design of CaPaMan (Cassino Parallel Manipulator) with a specified orientation workspace," *Robotica* **20**(2), 159–166 (2002).
[20] O. Altuzarra, C. Pinto, B. Sandru and A. Hernandez, "Optimal dimensioning for parallel manipulators: Workspace, dexterity, and energy," *J. Mech. Design*. **133**(4), 041007 (2011).
[21] Y. J. Zhao, "Dynamic optimum design of a 3UPS-PRU parallel robot," *Int. J. Adv. Robot. Syst*. **13**, (2016).
[22] Y. J. Zhao, "Dynamic optimum design of a three translational degrees of freedom parallel robot while considering anisotropic property," *Robot. Cim-Int. Manuf.* **29**(4), 100–112 (2013).
[23] M. H. Gholami and M. R. Azizi. "Constrained grinding optimization for time, cost, and surface roughness using NSGA-II," *Int. J. Adv. Manuf. Tech*. **73**(5–8), 981–988 (2014).

Cite this article: J. Wu, X. Wang, B. Zhang and T. Huang (2021). "Multi-objective optimal design of a novel 6-DOF spray-painting robot", Robotica **39**, 2268–2282. https://doi.org/10.1017/S026357472100031X